(RESEARCH ARTICLE)

Microstructure evolution and corrosion behaviors of cold-rolled 304 stainless sheets of steel in 3.5% NaCl solution

Isabella Teixeira Rezende [1], Erlan Samuel Santos [1], Wilian da Silva Labiapari [2], Elaine Carballo Siqueira Corrêa [1] and Marcello Rosa Dumont [1, *]

[1] Department of Materials Engineering, Federal Center for Technological Education of Minas Gerais (CEFET-MG), Av. Amazonas, 5253, Nova Suíça, Belo Horizonte, MG, Brasil - CEP: 30421-169.
[2] Aperam South America, Praça 1º de Maio, 9, Centro, Timóteo, MG, Brasil - CEP 35180-018.

Abstract

Austenitic stainless steel (ASS) is widely used in engineering applications due to its good corrosion resistance and mechanical properties. Several studies have indicated that the deformation-induced transformation of martensite in ASS significantly affects its corrosion resistance. However, corrosion resistance behavior in chloride-rich environments is more complex, and different cold-working methods have distinct impacts on localized corrosion. This study investigated the structural and corrosion resistance changes induced by cold rolling in AISI 304 samples. The used samples were initially subjected to a cold-rolling process with a thickness reduction of up to 50%. The results demonstrate an increase in the deformation-induced martensitic transformation and micro-hardness as the level of cold deformation increases. However, higher levels of deformation lead to the fragmentation of the formed α'-martensite lath structure into smaller laths, ultimately resulting in a predominantly refined and diffuse dislocation-cell-type structure. Potentiodynamic tests were conducted to analyze conventional electrochemical parameters, revealing a reduction in corrosion resistance with increasing cold deformation. This suggests that the formation, amount, and microstructure of α'-martensite, under imposed strain conditions, induce changes in the studied electrochemical parameters. Additionally, the more deformed samples exhibited a higher current density during passive layer formation, and exhibited more intense metastable pits, suggesting decreased corrosion resistance with higher degrees of deformation.

Keywords: Austenitic Stainless Steel; Potentiodynamic Polarization; Cold-Rolling Process; Deformation-Induced Martensitic Transformation

1. Introduction

Austenitic stainless steel (ASS) is widely utilized in various engineering applications, such as automotive, chemical, and marine industries (1), orthopedic (2) and orthodontic implants (3), nuclear power technology (4), petroleum, and gas exploration pipelines (5), pollution controls industries (6) and structural purposes in construction (7). The extensive use of ASS is attributed to its remarkable corrosion resistance, good mechanical properties, high ductility, and weldability. Previous research has demonstrated that these mechanical properties can be enhanced through fine-grain strengthening, phase transformation strengthening, and work hardening (8).

Cold-rolling and annealing processes are commonly employed as work hardening methods on ASS, resulting in increased yield strength and hardness in these alloys (9). However, it is crucial to acknowledge that work hardening can induce changes in the microstructure and potentially modify the corrosion resistance (10).

* Corresponding author: Marcello Rosa Dumont

Many studies have been performed to investigate the work hardening mechanism, mechanical properties, corrosion behavior (11), and microstructure evolution (12) during the cold deformation of ASS. Plastic deformation in ASS typically results, in its microstructure, in an increase in dislocation density, the formation of deformation bands, twining, and deformation-induced martensite on ASS. However, despite the published research, no general model describing the influence of the cold-deformation process on corrosion resistance in these steels is yet to be established, and contradictory results have been presented (13). The influence of factors, such as grain size, surface roughness, dislocation density, residual stress, and chemical uniformity on corrosion resistance, has been explored in several studies (14; 15; 16; 17). However, the findings have been inconsistent, with some studies indicating an increase in corrosion resistance, others suggesting a reduction, and some showing no significant change in this characteristic. The varying experimental conditions of cold working employed in these studies may contribute to the discrepancies in results. Distinct methods to induce microstructural modifications were used in each conclusion reported (18). In metastable austenitic steels, it is usually admitted that the corrosion resistance in acidic environments can be changed by the presence of martensite and the accumulation of dislocations induced by cold working. However, when exposed to a chloride-rich media, the corrosion resistance becomes more complex, and the localized corrosion is affected differently by each cold-working method. Reported studies involving more severe deformations have suggested a strong correlation between the degree of deformation and electrochemical potential alterations. Nevertheless, different findings it has also been reported. For example, some studies indicated that the pitting potential decreased, increased, or was unaffected as a result of a cold-working process or chloride concentration (19). Pitting corrosion represents a dangerous form of localized corrosion and can act as a precursor of stress corrosion cracking or fatigue failure (20). Its occurrence is influenced by a combination of electrochemical and metallurgical factors, including the presence and amount of alloying elements and the nature and distributions of non-metallic inclusions (15). Both the microstructure and chemical composition of ASS has been reported as key parameters for tailoring its mechanical properties and corrosion resistance (21). Therefore, the use of corrosion potential and pitting potential as a single criterion for defining the corrosion resistance of stainless steel does not provide a practical and reliable conclusion (19).

In this work, the effects of cold rolling, without subsequent annealing steps, on mechanical properties, corrosion behavior, and microstructure of commercial ASTM A240 Type 304 specimens, were investigated. The primary objective of excluding heat treatment after deformation was to observe the resultant effect on the material, closely corresponding to that typically observed in conventional mechanical forming processes, such as stamping or bending. These investigations were conducted under the influence of a common electrolyte solution. The study sought to analyze effects in hardness, corrosion behavior (e.g., pitting resistance, corrosion rate), and microstructure. By observing these effects, valuable insights can be gained into the behavior of the material under imposed conditions. Unidirectional cold rolling was performed on a 3.0mm thick commercial sample to obtain specimens with thickness reductions of 10%, 20%, 30%, 40%, and 50%. The resulting samples underwent analysis with optical emission spectroscopy and Infrared absorption for elemental analysis, X-ray diffraction for phase identification, optical microscopy for microstructural characterization, and potentiodynamic polarization for investigating the corrosion behavior.

2. Material and methods

2.1. Materials

A commercial hot-rolled and annealed plate of ASS, ASTM 304 grade, with 3.0mm of thickness was used as started material. The chemical composition of the samples is summarized in Table 1. Carbon and sulfur content was determined using a Leco model CS444 Infrared Absorption equipment. Nitrogen content was analyzed using Leco TC436 Thermal Conductivity equipment. Additionally, the content of all other chemical elements was determined by ThermoARL 4460 Optical Emission Spectrometry equipment.

Table 1 Chemical composition of ASTM 304 as-received austenitic stainless steel (weight %)

Composition (%)	C	Mn	P	S	Si	Cr	Ni	N
ASTM A240 – 304 type	< 0.08	< 2.00	< 0.045	< 0.03	< 0.75	18.0 – 20.0	8.0 – 11.0	< 0.10
Sample	0.02	1.28	0.040	0.001	0.40	18.0	8.0	0.04

The obtained chemical compositions are consistent with the specifications outlined for 304 ASS in the ASTM A240 standard (22). It is well-documented that an increase in the content of chromium and molybdenum content usually results in heightened resistance against general corrosion, pitting, and crevice corrosion. Furthermore, elevated levels

of nickel in the alloy enhance its resistance to stress cracking, while low carbon levels in the material provide resistance to intergranular corrosion (23).

The pitting resistance equivalent number (PREN) is a well-known parameter for stainless steel corrosion assessment. It utilizes the chemical composition of the alloy to predict its resistance to localized pitting corrosion, with the formula PREN=%Cr+3.3%Mo+16%N. PREN serves as a valuable tool for material selection and design considerations, as it enables the estimation of pitting resistance based on the alloy's composition. The calculated PREN value aids in assessing the suitability of the stainless steel for applications prone to pitting corrosion in various environments (24; 25). In the present study, the tested samples exhibited a PREN value of 18 aligning with the expected range for this material (26).

2.2. Sample preparation

Successive unidirectional cold-rolling passes were employed in the Duo Quadruo laminator to achieve thickness reduction of 10%, 20%, 30%, 40%, and 50%. It is important to note that no annealing heat treatment was performed subsequently to the cold-rolling processes to maintain the resemblance of deformed samples to those obtained through conventional mechanical forming techniques. Square samples were then cut from each thickness reduction group, with dimensions of 10mm x 10mm x final thickness, utilizing an electric guillotine Newton TM10.

To analyze the microstructure and microhardness, a standard hot mounting metallographic preparation technique was performed. The samples were sanded from 120-grit to 600-grit with silicon carbide papers, then polished with 9μm and 3μm diamond paste, and finally rinsed with ethanol solution (5). To conduct the electrochemical tests the samples were previously submitted to the passivation process with nitric acid, following the guidelines outlined in ASTM A967. This passivation step aimed to minimize the impact of interstitial corrosion during the subsequent polarization tests. Subsequently, the samples were cold-mounted in self-curing acrylic resin, with a copper wire connected to the inner face. To mitigate the influence of surface roughness on corrosion performance, the previously described grinding and polishing metallographic preparation method was employed.

2.3. Microstructural characterization

The samples were subjected to immersion in a freshly prepared aqua regia acid solution (1:3 volume ratio of concentrated HNO_3 – 65% Syhth: concentrated HCl – 37% Synth) for a few seconds. Following the acid passivation, the samples were thoroughly rinsed with distilled water and ethanol. The microstructure on the polished and attacked cross-section of each sample was then examined using the optical microscope Fortel-IM713 model with various magnifications.

X-ray diffraction (XRD) analysis was performed using a Shimadzu XRD-7000 diffractometer. The experimental parameters were set at a step size of 0.02°, scan range 2-theta from 40° to 100°, scan speed of 2°.min^{-1} and operating at 40kV and 30mA. Cuk$_\alpha$ was used as the radiation source. Before the analysis, the samples underwent immersion in a hydrochloric acid solution. This step was carried out to remove the oxidized passive layer present on the surface, thereby minimizing the influence of any oxide species during the XRD analysis. The quantitative estimations of volume fraction $V_{\alpha'}$ and V_γ were determined by analyzing the integrated intensities of the peaks corresponding to the γ-austenite phases and deformation-induced α'-martensite phases obtained on XRD. This approach is grounded on the principle that the quantitative estimation of phase is directly proportional to the total integrated intensity of all diffraction peaks associated with that particular phase. The volume fraction $V_{\alpha'}$ and V_γ can be derived for numerous peaks as given in equation (1) and equation (2),

$$V_i = \frac{\frac{1}{n}\sum_{j=1}^{n}\frac{I_i^j}{R_i^j}}{\frac{1}{n}\sum_{j=1}^{n}\frac{I_\gamma^j}{R_\gamma^j}+\frac{1}{n}\sum_{j=1}^{n}\frac{I_{\alpha'}^j}{R_{\alpha'}^j}} \quad ....(1)$$

$$V_{\alpha'} + V_\gamma = 1 ....(2)$$

where I = peak integrated intensity i = γ or α', n = number of examined peaks, and R = the calculated theoretical intensity for the (hkl) plane of the i-phase. Equations 1 and 2 allow a concurrent determination of the volume fraction of γ-austenite and α'-martensite present in austenitic stainless steel using XRD analysis. This is achieved by measuring the integrated intensity of each peak corresponding to these phases (27; 28).

2.4. Mechanical properties

The Vickers micro-hardness measurement was conducted at room temperature using a Shimadzu HMW 2T micro-hardness test instrument. A load of 4.903N was applied for a dwell time of 15 seconds. To ensure representative results, ten measurements were taken at random regions on each sample, and the average hardness values were recorded. The Vickers Hardness Number (Hv) was calculated using a standard equation 3 (29),

$$Hv = 1.8544 \frac{P}{d^2} \dots\dots\dots\dots\dots \text{(3)}$$

where P is the applied load and d is the diagonal length obtained from the indenter impression.

2.5. Corrosion resistance

The corrosion behavior of all samples was assessed through a potentiodynamic polarization test performed at room temperature. A standard 3.5% NaCl solution (30; 31; 32) was used as an electrolyte. The electrochemical measurements were repeated at least three times for each sample to ensure result consistency and statistical significance. The tests were carried out in a Vertex 100 mA. EIS potentiometer, employing a 3-electrodes electrochemical cell system (33). An Ag/AgCl electrode was used as the reference electrode, a high-purity platinum wire was used as the counter electrode and the samples were used as the working electrode. Before conducting the electrochemical measurements, the open circuit potential (OCP) was determined by immersing the samples in the electrolytic solution for 3600s to form a stable passive film on the surface of the samples (34). Potentiodynamic polarization tests were performed with a sweeping range starting from -0.25V$_{(vs\ Ag/AgCl)}$, relative to OCP value, and extending up to 1.20V$_{(vs\ Ag/AgCl)}$. The sweep rate employed was 0.6V.h^{-1} (30; 35). This sweep rate was selected to maintain relatively stable corrosion conditions throughout the potentiodynamic polarization tests. This rate allows for a controlled and gradual change in potential, ensuring reliable and consistent measurements of the corrosion behavior (36). Quantitative data were obtained for the corrosion current density (I$_{corr}$) and corrosion potential (E$_{corr}$) by determining the point of interception between the tangent line of the cathodic branch with the tangent line of the anodic branch in the potentiodynamic polarization curves (37). Anodic Tafel constant (βa) and cathodic Tafel constant (βc), which describe the rate of the anodic and cathodic reactions, critical pitting potential (E$_{pit}$), and corrosion rate were also obtained. Anodic and cathodic branches were considered, for Tafel constants, within a range approximately 0.10V higher and 0,10V lower than the OCP value. This range ensures that the relevant regions of the polarization curves are captured for accurate estimation of the Tafel constants.

3. Results and discussion

### 3.1. Microstructural characterization

The optical micrographs obtained are shown in Figure 1. The microstructural analysis revealed a characteristic austenitic structure (33) in the as-received samples (Figure 1 (a)). The microstructure exhibited equiaxed and annealing twinning grains (12) indicating that recrystallization phenomena have fully occurred. Elongated austenitic grains are observed, stretched severely as the deformation increased, containing deformation twins and a gradual formation of α'-martensite (Figure 1 from (b) to (f)) suggesting that the deformation-induced martensitic transformation occurred during cold deformation. The resulting microstructure observed consists of α'-martensite and partially deformed austenite. The initiation of deformation-induced martensite is evident through the formation of acicular structures resembling needles (27; 38), within the grains, as indicated by the arrows in Figure 1 (a) and (b). Martensite formation occurs as a result of localized plastic deformation, leading to the development of needle-like structures. These needles are formed at activated slip systems and within the plastic zone of emerging short cracks. This structure, as depicted more prominently in Figure 1 (b), is characteristic of lath-type martensite. However, as the deformation increased, the lath-type structure underwent fragmentation into smaller laths. Ultimately, a predominantly dislocation-cell-type structure was formed (8), as demonstrated in Figure 1 (c) – (f). As the percentage of thickness reduction gradually increased, reaching 50%, there was an increase in the content of martensite. The morphology of martensite became more diffuse and dispersed, as observed in other works (11). The grains in the microstructure transformed into a long-striped shape and the grain's boundaries became less distinct. No precipitates or other structures were found in the analyzed samples.

The XRD profiles of the samples are presented in Figure 2. Individual and free of adjoining diffraction peaks are clearly observed for α'-martensite (bcc) and γ-austenite (fcc), indicating that they exist as separate and distinct phases without any overlapping diffraction peaks from adjacent phases. The diffraction peaks observed in the analyzed ASS samples and their associated planes can be identified as (39; 40) γ-(111), γ-(200), γ-(220), γ-(311), and γ-(222) at 2θ of 43.6°, 50.9°, 74.8°, 90.0°, and 96.0°, respectively, and as α'-(110), α'-(200) and α'-(211) at 2θ of 44.6°, 65.0°, and 82.1°,

respectively. As the thickness reduction increases, there is a gradual reduction in the peaks corresponding to the austenitic phase. In the sample with a 50% thickness reduction, these peaks are almost completely diminished. Conversely, the peaks corresponding to the martensitic phase, which are not initially observed in the as-received sample, show a gradual increase in intensity. Room temperature deformation results in a prominent increase in the peak intensity of the α'-martensite (110), (200), and (211) planes, as observed in deformed samples. ASS is known to be metastable, and plastic deformation resulting from monotonic or cyclic loading can induce a diffusionless transformation of the γ-austenitic phase to the α'-martensitic phase. The presence and amount of α'-martensite induced by plastic deformation in ASS lead to a change in its physical and chemical properties. Indeed, the presence of both martensite and austenite phases in austenitic stainless steel can create a potential for galvanic corrosion due to the difference in their corrosion potentials. However, the occurrence of galvanic corrosion depends on several factors, including plastic strain, strain rate, stress rate, deformation mode, grain size, and grain orientation. These factors can influence the extent and severity of galvanic corrosion in the material. Additionally, the presence of martensite in austenitic stainless steel contributes to increased hardness and ultimate tensile strength. Martensite is generally harder and stronger than austenite, and its presence can enhance the mechanical properties of the material.
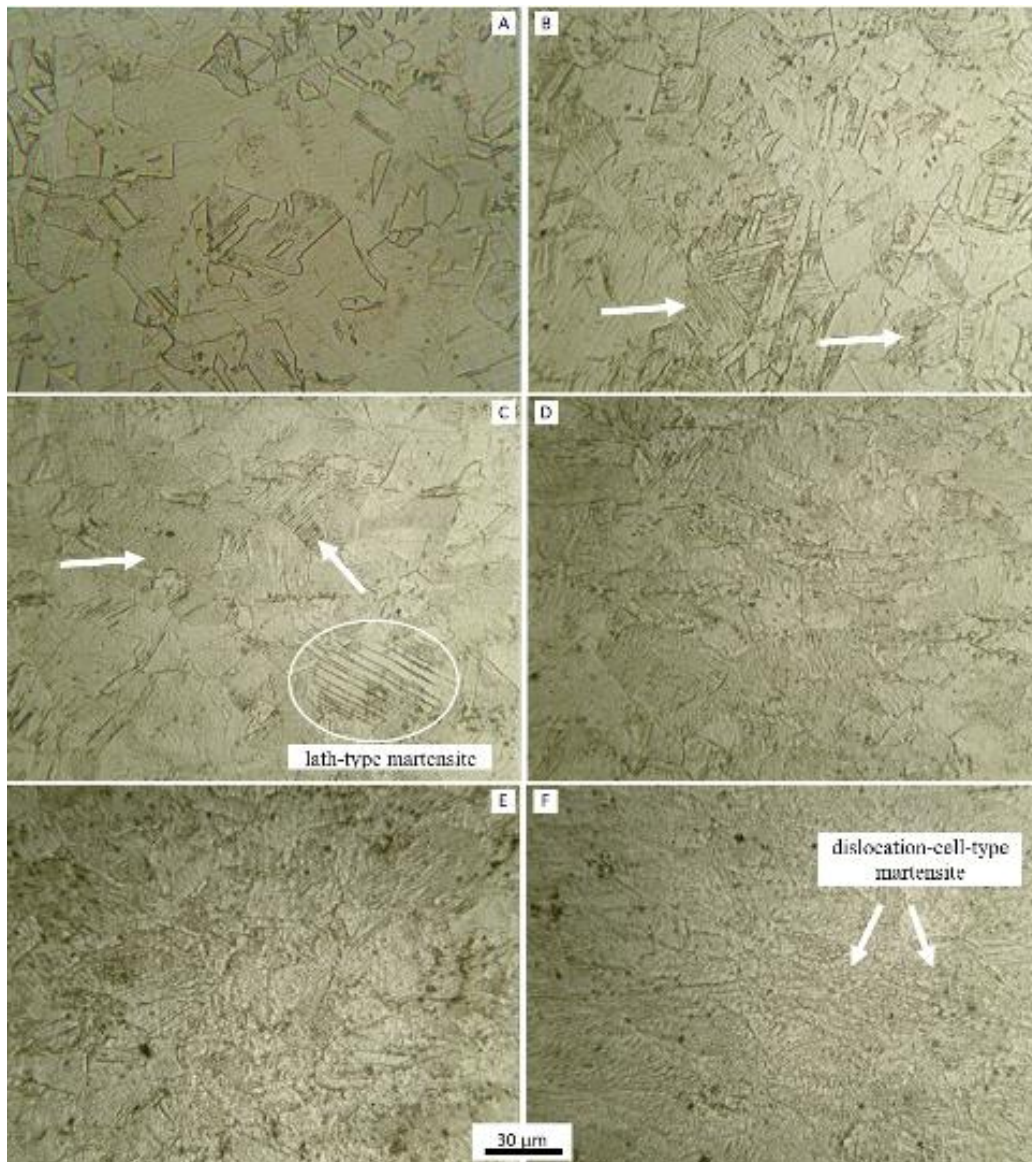
Figure 1 Micrographs obtained for 304 stainless steels etched in aqua regia solution: (a) as received, (b) 10% of thickness reduction, (c) 20% of thickness reduction, (d) 30% of thickness reduction, (e) 40% of thickness reduction and (f) 50% of thickness reduction
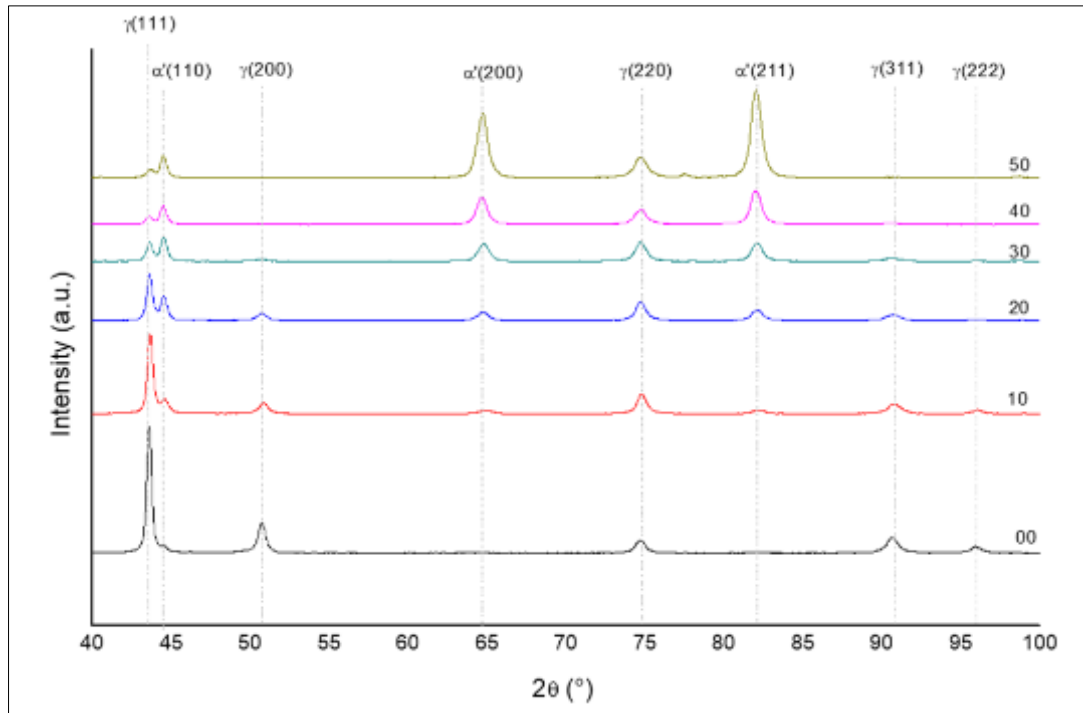
Figure 2 X-ray diffraction patterns for analyzed cold-rolled 304 ASS with different thickness reductions

The XRD analysis conducted on both the as-received and cold-deformed ASS samples allowed for the identification of the distinct phases present in their structure. It confirmed the occurrence of a gradual deformation-induced martensitic transformation, which was previously observed through optical microscopy (Figure 1). This result supports the conclusion that the emergence of martensite in ASS occurred due to cold plastic deformation. The absence of ε-martensite (hexagonal close-packed, hpc) (28) phase in the analyzed samples suggests that the reaction of γ-austenite to ε-martensite to α'-martensite (41) is either complete or that the cold-deformation generated only the γ-austenite to α'-martensite transformation (42). Li et al. (40) demonstrated that in 304 ASS with small cold-rolling thickness reduction, martensite transformation occurs through both mentioned paths. However, with greater deformations, the transformation from γ-austenite to α'-martensite predominates, and the grain boundaries are largely broken, forming with more slip systems, while martensite nucleated and grew everywhere, as is observed (Figure 1) on cold-rolled analyzed samples in this work. α'-martensite is formed as a result of shear band intersections and dislocation pileups, a mechanism commonly present in cold-rolling, while ε-martensite nucleates at stacking faults (28). The deformation-induced martensitic transformation involves a sudden reorientation of carbon and iron atoms within a face-centered cubic structure (austenite), resulting in the formation of a body-centered cubic structure (martensite). This transformation is influenced by several factors, including the magnitude of strain, temperature, strain rate, strain state, and grain size. The proportional volume fraction of martensite and austenite was also estimated through X-ray diffraction analysis of the investigated specimens. The quantitative volume fraction of each phase was estimated using equation 3 using all identified peaks of martensite and austenite (41). The resulting values are shown in Table 2 and visually depicted in Figure 3. It is evident that the volumetric fraction of austenite, initially 1.00, undergoes a gradual transformation into martensite due to cold deformation, ultimately decreasing to 0.18 in the sample subjected to a 50% reduction in thickness. Since no other distinct phases were observed, it can be concluded that the volumetric fraction of martensite increases from 0.00 to 0.82. This progressive outcome aligns consistently with each increment of thickness reduction and supports the microstructure observed through optical microscopy.

Table 2 Estimated volumetric fraction phase of ASTM 304 austenitic stainless steel in different cold-rolling deformations

Thickness reduction (%)	00	10	20	30	40	50
Austenite	1.00	0.88	0.62	0.42	0.21	0.18
Martensite	0.00	0.12	0.38	0.58	0.79	0.82
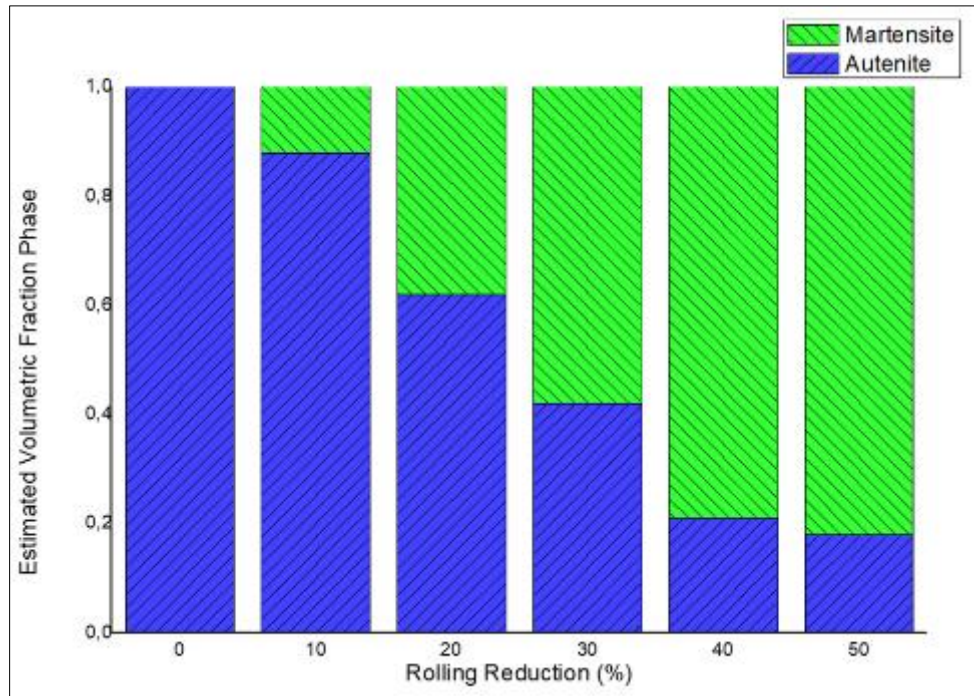
Figure 3 Estimated volume fraction of austenite and martensite phases for cold-rolled 304 stainless steel with different thickness reduction

3.2. Vickers micro-hardening

The results obtained from the Vickers micro-hardening test are summarized in Table 3 and graphically presented in Figure 4. Consistent with expectation (43), it is observed that micro-hardness tends to increase, starting from 212HV +/- 6HV on the as-received sample to 433HV +/- 7HV on the sample subjected to a 50% reduction in thickness, representing an increase of 104%. Furthermore, these results exhibit a gradual progression that corresponds to the increasing deformation, which is consistent with the observed augmentation of martensite presence and content as identified through XRD and optical microscopy. The notable increase in micro-hardness can be attributed to the development and amplification of deformation-induced martensite, as well, as the work-hardening effect (39). This can be explained by the rise in dislocation density within the austenite phase, impeding dislocation movement and making deformation more difficult.
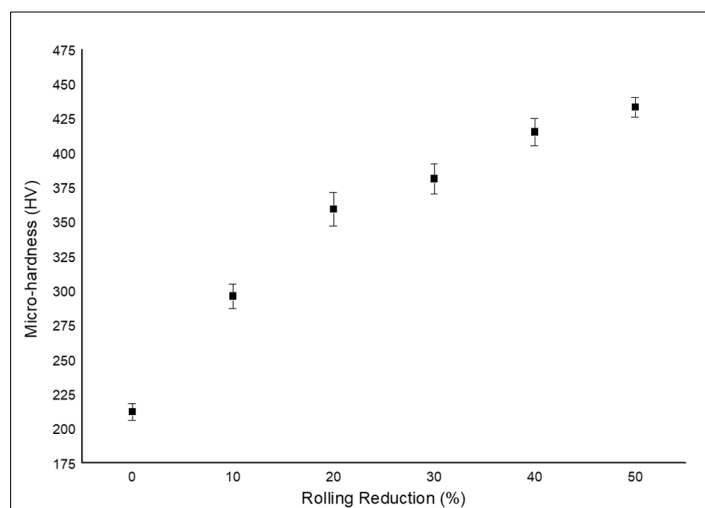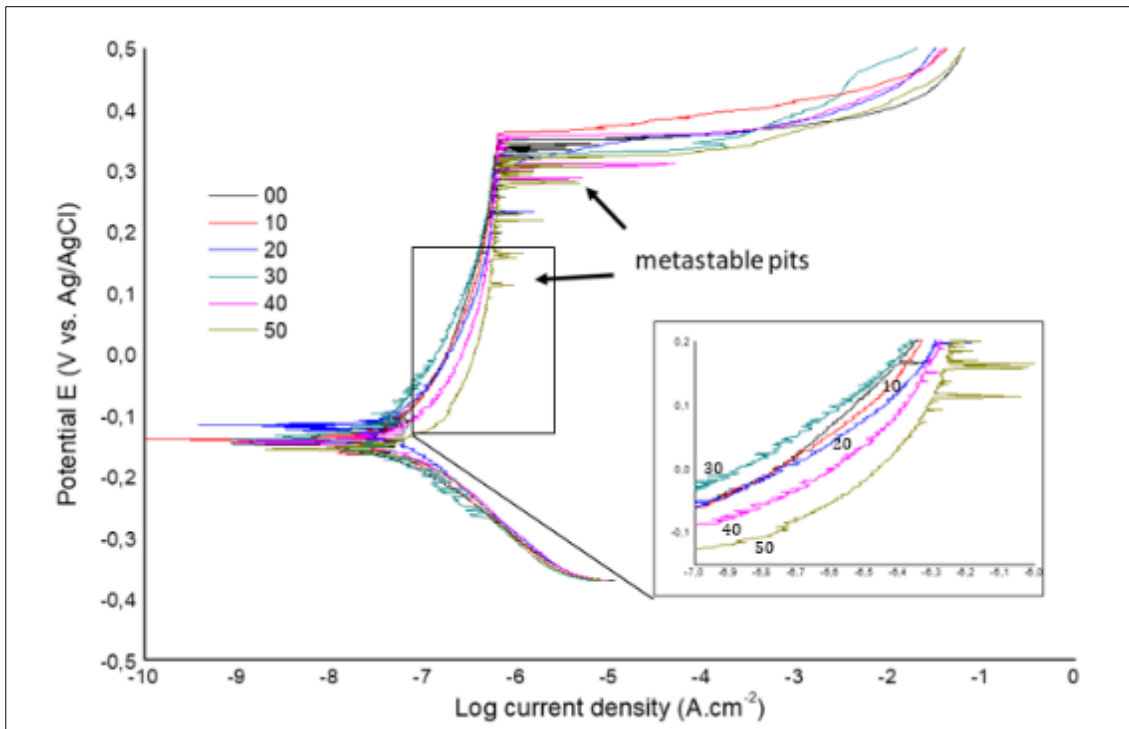

Figure 4 Vickers micro-hardening of cold-rolled 304 stainless steel with different thickness reductions (applied load of 4.903N for 15s)

Table 3 Vickers micro-hardness results of ASTM 304 with different cold-rolling deformations

Thickness reduction (%)	00	10	20	30	40	50
Micro-hardness (HV)	212 +/- 6	296 +/- 9	359 +/- 12	381 +/- 11	415 +/- 10	433 +/- 7

3.3. Corrosion resistance

Figure 5 Potentiodynamic polarization curves obtained for cold-rolled 304 stainless steel with different thickness reductions

Similar OCP curves were observed for all analyzed samples. The OCP values exhibit a gradual stabilization over time, with an overall increase. This trend suggests the formation of a spontaneous passive film on the surface. After a stabilization time of 3600s, potentials between $-0.10V_{(vs\ Ag/AgCl)}$ and $-0.15V_{(vs\ Ag/AgCl)}$ were observed. Figure 5 depicts the representative potentiodynamic polarization curve, E vs log $|i|$, for all examined specimens. Typical and expected (44) polarization curves were obtained for 304 stainless-steel analyzed samples. In these curves the cathodic branches indicate the process of cathodic decomposition of water, resulting in the formation of hydroxyl groups and hydrogen (45), and the anodic branches indicate the anodic dissolution of stainless-steel samples. The transition region from the active zone to the passive zone is not clearly evident on the anodic branches. However, it is observed that the anodic branch exhibits a steeper slope compared to the cathodic branch, indicating the onset of passivation shortly after the corrosion potential. Therefore, the active-passive behavior can be observed in all anodic branches. The transition region from the active to a passive state, which is considered a critical passivation current (24), is observed more prominently in samples with higher deformation. In these samples, the transition region occurs at higher current values, specifically at 0.183μA for the sample with a 50% thickness reduction and 0.052μA for the sample with a 10% thickness reduction. This suggests that lower deformed samples offer greater protection (46).

Metastable pits in the passive zone, as indicated by the arrows in Figure 4, were observed on analyzed samples starting from a potential of $0.10V_{(vs\ Ag/AgCl)}$. These pits were evidenced by current spikes or instabilities (47) predicting their initiation and subsequent repassivation. As the cold deformation increased, these pits became more frequent and exhibited greater current oscillations. This observation suggests that the increase in cold deformation leads to the formation of more microstructural irregularities, providing potential nucleation sites for the metastable pits. It has been established that the behavior of metastable pits is closely linked to factors such as potentials, environmental conditions, and the microstructure of the alloy. These factors significantly influence the formation, growth, and stability of metastable pits, ultimately affecting the overall corrosion behavior of the material (44). In the analyzed ASS samples, the microstructure (Figure 1) reveals the presence of the α'-martensitic phase, which undergoes a gradual

transformation from lath-type to a dislocation-cell-type morphology. Although the α'-martensite is more diffused and more dispersed, which could potentially enhance resistance to metastable pitting by reducing surface heterogeneities, the higher fractions of α'-martensite have a negative impact on the formation of the passive layer. This, in turn, allows for the formation of more pronounced metastable pits at lower potentials, as observed in the sample with 40% and 50% thickness reduction. The higher presence of α'-martensite appears to disrupt the formation and stability of the passive layer, thereby promoting the occurrence of more aggressive metastable pitting. These results provide further support for the notion that the occurrence of metastable or stable pitting corrosion is primarily dominated by the protective ability of the passive film formed during the polarization phase rather than during the cold-forming process. Stable pitting is observed at approximately $0.3V_{(vs\ Ag/AgCl)}$ characterized by a sudden and pronounced increase in current density from the passive current density levels of around $0.5\mu A.cm^{-2}$. These values are consistent with those reported for 304 ASS in saline media (48), indicating a good general corrosion resistance in this environment.

Pitting corrosion is indeed the most common corrosion mechanism observed in stainless steel when exposed to chloride ions. This type of corrosion mechanism is typically induced by the presence of chloride anions in neutral or acid-aggressive solutions. Chloride anions are known to play a critical role in the depassivation of stainless steel. The passive film becomes unstable when chloride ions replace oxygen ions held within the passive layer, causing a difference in chemical potential across the film (23). Pitting corrosion on stainless steel typically develops in three stages: nucleation, metastable growth, and stable growth. Metastable pits are initially small and can become stable at higher potentials (14). Pitting corrosion often occurs at sites of heterogeneities on the metal surface, by the galvanic coupling between distinct phases or regions with varying electrochemical potentials, which are susceptible to corrosion initiation, stabilization, and propagation. Local composition and crystallographic heterogeneities are the dominant factors promoting corrosion on stainless steel (austenitic, ferritic, martensitic, or dual phase). It is widely accepted that pits tend to nucleate at carbides, grain boundaries, flaws, dislocations, and other heterogeneities on the metal surface structure. The presence of these heterogeneities creates conditions conducive to localized and preferential attack, thereby exacerbating the corrosion process. Contrarily, certain studies have suggested that cold work enhances the resistance to pitting corrosion due to increased diffusion of chromium. This subsequently leads to the thickening of the passive layer providing a protective barrier against corrosion (49). The present study did not observe any evidence of precipitates or the formation of significant heterogeneities within the microstructure of the analyzed samples. The obtained martensite exhibits a highly dispersed microstructure within the grains, without the presence of an island of discontinuity or a grain isolated from the austenitic structure. It can be inferred that the microstructure, despite the increasing presence of the martensite phase, remained relatively homogeneous.

Table 4 Potentiodynamic polarization parameter of ASTM 304 with different cold-rolling deformations obtained in 3.5% NaCl solution at room temperature

Thickness reduction (%)	00	10	20	30	40	50
E_{corr} (V $_{vs\ Ag/AgCl}$)	-0.14 +/- 0.03	-0.15 +/- 0.02	-0.14 +/- 0.01	-0.13 +/- 0.02	-016 +/- 0.01	-0.15 +/- 0.03
i_{corr} ($\mu A.cm^{-2}$)	0.05 +/- 0.01	0.01 +/- 0.02	0.03 +/- 0.01	0.02 +/- 0.02	0.04 +/- 0.01	0.04 +/- 0.01
E_{pit} (V $_{vs\ Ag/AgCl}$)	0.32 +/- 0.03	0.35 +/- 0.01	0.27 +/- 0.05	0.27 +/- 0.08	0.29 +/- 0.03	0.36 +/- 0.06
β_a (V.dec^{-1})	0.17 +/- 0.06	0.12 +/- 0.01	0.15 +/- 0.05	0.14 +/- 0.05	0.17 +/- 0.05	0.25 +/- 0.09
β_c (V.dec^{-1})	0.10 +/- 0.09	0.09 +/- 0.01	0.10 +/- 0.01	0.09 +/- 0.02	0.09 +/- 0.01	0.09 +/- 0.02
Corrosion rate ($\mu m.y^{-1}$)	0.55 +/- 0.09	0.35 +/- 0.01	0.40 +/- 0.08	0.32 +/- 0.01	0.50 +/- 0.09	0.50 +/- 0.09

Table 4 presents detailed quantitative values obtained through data fitting of potentiodynamic polarization curves. These values include corrosion potential (E_{corr}), corrosion current density (I_{corr}), critical pit potential (E_{pit}), Tafel constants (β_a and β_c), and corrosion rate. Figure 6, Figure 7, and Figure 8 graphically illustrate these values. E_{corr} average values are found from $-0.13V_{(vs\ Ag/AgCl)}$ to $-0.16V_{(vs\ Ag/AgCl)}$. These results demonstrated a good correlation with the obtained OCP values. Previous studies on 304 stainless steels (47) have reported differences of approximately 50mV in corrosion potential values for the same material. These findings provide additional support and validation for the results obtained in the present study. The observed variations in corrosion potential values between different studies are primarily attributed to the scan rates utilized in each experiment. It is recommended that scan rates for Tafel experiments be set at $0.5mV.s^{-1}$ or below. The obtained I_{corr} values ranged from $0.01\mu A.cm^{-2}$ to $0.05\mu A.cm^{-2}$. In this study, the potential at which a continuous and rapid increase in current occurs after the occurrence of metastable pitting was identified as the stable pit region and defined as the critical pitting potential. E_{pit} values were observed to range from

$0.27V_{(vs\ Ag/AgCl)}$ to $0.36V_{(vs\ Ag/AgCl)}$, which is consistent with results from other studies on 304 stainless steel. Additionally, the corrosion rate values ranged from $0.32\mu m.y^{-1}$ to $0.55\mu m.y^{-1}$. Furthermore, higher values of βa compared to βc were observed, indicating an acceleration of the passivation process (50). This suggests that the anodic reaction, associated with the formation of the passive layer, occurs at a faster rate than the cathodic reaction, thereby contributing to the overall enhancement of the passivation phenomenon.
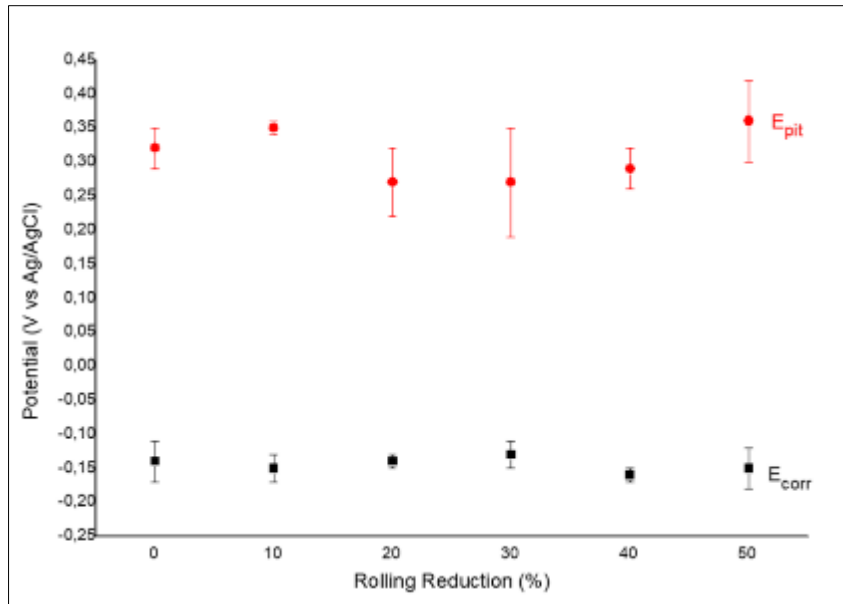
Figure 6 Corrosion potential (E_{corr}) and pit potential (E_{pit}) obtained for cold-rolled 304 stainless steel with different thickness reduction, calculated from potentiodynamic polarization test
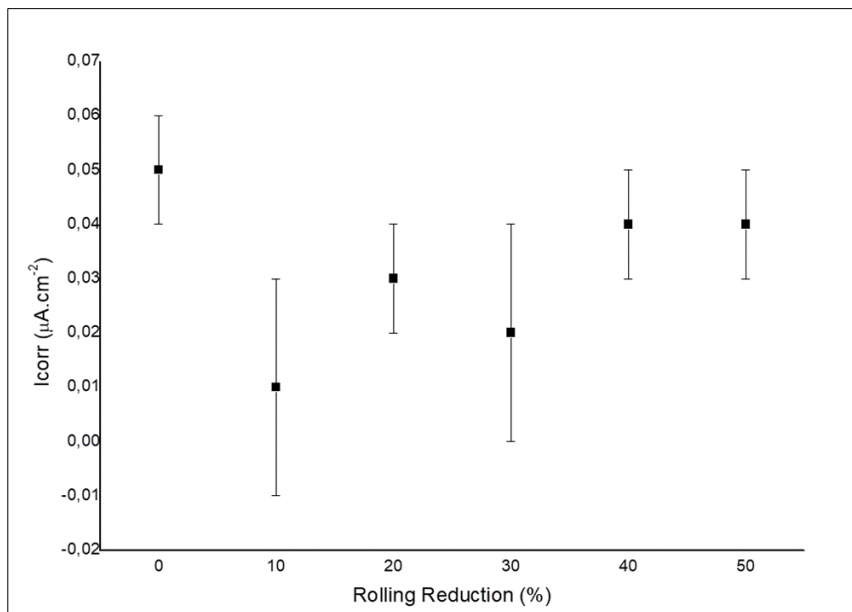
Figure 7 Corrosion current density (I_{corr}) obtained for cold-rolled 304 stainless steel with different thickness reduction, calculated from potentiodynamic polarization test
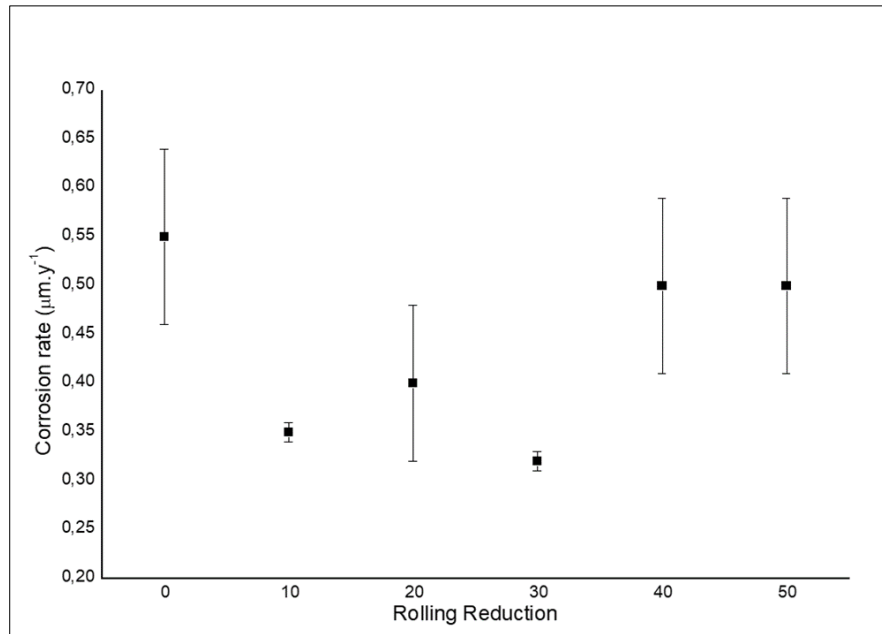
Figure 8 Corrosion rate obtained for cold-rolled 304 stainless steel with different thickness reduction, calculated from potentiodynamic polarization test

Contradictory evidence regarding corrosion resistance has been reported about the presence or the absence of process-related defects, cracks, porosities, and deleterious secondary phases, impacting the characteristics of the passive film (51; 52). Analyzing the parameters E_{corr}, I_{corr}, and E_{pit}, presented in Table 4, which are typically employed as key parameters to assess the corrosion resistance of ASS, there is no strong indication of a significant relationship between the obtained values and the amount of cold deformation. It is important to consider that the sample without deformation in this study was commercially supplied with annealing, whereas the cold-rolled samples did not undergo any heat treatment after the cold-rolling step. The presence of annealing in the commercially supplied sample can introduce changes in the microstructure and mechanical properties, potentially affecting the corrosion behavior. The absence of heat treatment in the cold-rolled samples means that the effects of strain hardening and residual stresses resulting from the deformation process might influence the corrosion resistance differently. Therefore, a direct comparison of these samples could lead to misinterpretation. By focusing on the analysis of the cold-rolled deformed samples, those with 10% to 50% thickness reduction, where the presence of martensite is observed, trends can be observed in the data. Figure 6 indicates a small, discrete, and gradual increase in the average value of E_{corr} as the deformation level increases, particularly in the range of 20% to 50% deformation. This suggests that higher deformation levels may lead to slightly more positive corrosion potentials and potentially improved corrosion resistance. Furthermore, Figure 7 demonstrates a correlation between the average values of I_{corr} and increased deformation. As the deformation level increases, there is a more evident increase in the average values of I_{corr}. This implies a higher corrosion rate and reduced corrosion resistance with increasing deformation. This trend is further supported by Figure 8, which shows similar behavior in the average values of corrosion rate as a function of increased deformation. The corrosion rate tends to increase gradually as the deformation level rises, indicating a decrease in corrosion resistance. The sample with 10% thickness reduction shows an average I_{corr} of $0.01 \mu A.cm^{-2}$ and corrosion rate of $0.35 \mu m.y^{-1}$ while the sample with 50% of thickness reduction shows an average I_{corr} of $0.04 \mu A.cm^{-2}$ and corrosion rate of $0.50 \mu m.y^{-1}$. As reported, the corrosion rate does not change significantly with cold rolling until 20% of thickness reduction (43), as observed in this present work. In their study, Ma et al (37) demonstrated a variation in corrosion current, over cold-rolling Ta-alloy, increasing the current until 50% of thickness reduction, and then reducing the current until 90% of thickness reduction, with the extremes 0% and 90% showing the same value. It is generally believed that cold deformation on alloys promotes changes in the microstructure and consequently in corrosion resistance. The increase in crystal defects caused by cold deformation tends to accelerate the corrosion process, however, other factors can influence corrosion behavior after deformation. These factors include the presence of heterogeneities such as precipitates (33), residual stress (34), secondary phase, heterogeneous stress and strain (53), and welded joints (54; 55). Therefore, while cold deformation is known to impact corrosion resistance, the specific influence can be influenced by multiple interconnected factors.

During plastic deformation, the passive film on the surface of a metal can be disrupted or broken, leading to the formation of the anodic area can form and preferential dissolution could occur. The oxidation reactions on the surface occur when the metal ions move from preferred surface sites toward the surrounding solution (44). The analyzed

samples were previously deformed and sanded, in sample preparation, removing any surface-formed oxide. Furthermore, during OCP measurements, a new continuous passive layer was formed. Thus, surface irregularities possibly caused by cold deformation were normalized. It is indicated by the values of potential and current density obtained that the formation of the passive layer occurred uniformly in all samples. Houmard and coworkers (56) demonstrated that the ratio $(Fe/Cr)_{oxide}$ (iron enrichment) increases with the cold-rolling process. This can then lead to variations in the corrosive behavior, however, this passive layer formed is removed in electrochemical tests and thus the effect of the cold-rolling passive layer is not analyzed. In this way, the results found are more related to the intrinsic corrosion resistance of the material with its microstructure than the changes in the passive layer generated during cold rolling.

Based on the results obtained in this work, a smooth trend and influence on corrosion resistance were observed, as expected, as a function of thickness reduction, within the analyzed thickness reduction range. Regarding the influence of cold rolling on corrosion behavior, subtle changes in typical corrosion behavior parameters (E_{corr}, I_{corr}, E_{pit}) were observed, contrary to some published data. But it was described that changes in corrosion resistance as a function of cold deformation are specific results for each deformation process employed (18). In addition, it was demonstrated that the more detailed analysis of the passive regions showed differences in the more deformed samples, in this analysis, showing a lower corrosion resistance. The evidence found, in this study, evidences a high corrosion resistance of the analyzed ASS, even with microstructural changes. It is important to highlight that these observed results are typical for passivating metals, and it means, that anodic dissolution is controlled by passive current density. Accordingly, the pitting potential values in the passivity region, the passive current densities, and their fluctuations, reflecting the presence of metastable pitting, have higher importance that the Tafel analysis results. Since the pitting potential values, in this study, do not change clearly depending on the cold deformations (Table 4), the metastable pit growth and passive current density changes are the most important indicators of corrosion resistance. Studies focused on the formation and density of metastable pits should be conducted to better understand this aspect.

4. Conclusion

The influence of cold-rolling deformation on ASTM 304 stainless steel is investigated through metallurgical and electrochemical characterization in the presence of a standard 3.5% NaCl electrolytic solution. The obtained results and discussions presented lead to the following conclusions:

- As expected, the initial microstructure of the samples consisted of a single austenitic phase which changes into deformation-induced martensite and austenite, due to γ-austenite $\rightarrow$ α'-martensite transformation. The deformed-induced transformations of martensite were strictly proportional to the imposed deformation.
- The microstructural changes observed in the cold-rolled samples, were homogeneous, without the formation of precipitates or defects. The formation of the passive layer under these conditions was not impaired, maintaining high corrosion resistance in all specimens.
- The results demonstrate a clear correlation between Vickers micro-hardness and α'-martensite content.
- The analysis of the passive region, on potentiodynamic polarization curves, showed higher current densities and the occurrence of metastable pits, which were more prominent in the more deformed samples. These results suggest that cold deformation has a negative effect on corrosion behavior, even when the typical potentiodynamic parameters do not exhibit clear trends in this regard. Therefore, a detailed analysis of the pit growth and stability needs to be better investigated.

Compliance with ethical standards

Disclosure of conflict of interest

The authors declare that they have no known competing commercial interests or personal relationships that could have appeared to influence the work reported in this paper.

Data availability

The raw data with the findings of this article cannot be shared since there is ongoing research.

References

[1] Das, A. K. Recent developments in TIG torch assisted coating on austenitic stainless steel: A critical review. *Materials Today: Proceedings.* 2022, Vol. 57, pp. 1846-1851. https://doi.org/10.1016/j.matpr.2022.01.077.

[2] Pathote, D., et al. Optimization of electrochemical corrosion behavior of 316L stainless steel as an effective biomaterial for orthopedic applications. *Materials Today: Proceedings.* 2022, Vol. 57, pp. 265-269. https://doi.org/10.1016/j.matpr.2022.02.501.

[3] Cheary, R. W. and Ma-Sorrell, Y. Quantitative phase analysis by X-ray diffraction of martensite and austenite in strongly oriented orthodontic stainless steel wires. *Journal of Materials Science.* 2000, Vol. 35, pp. 1105-1113. https://doi.org/10.1023/A:1004755514188.

[4] Lan, X., et al. Magnetic characteristics and mechanism of 304 austenitic stainless steel under fatigue loading. *Engineering Failure Analysis.* 2022, Vol. 136, p. 106182. https://doi.org/10.1016/j.engfailanal.2022.106182.

[5] Li, L., et al. A comparative study of corrosion behavior of S-phase with AISI 304 austenitic stainless steel in H2S/CO2/Cl- media. *Corrosion Science.* 2021, Vol. 187, p. 109472. https://doi.org/10.1016/j.corsci.2021.109472.

[6] Wang, W., et al. Microstructure and mechanical properties of dissimilar friction stir welds in austenitic-duplex stainless steels. *Materials Science & Engineering A.* 2020, Vol. 787, p. 139499. https://doi.org/10.1016/j.msea.2020.139499.

[7] Laukkanen, A., et al. Micromechanics driven design of ferritic–austenitic duplex stainless steel microstructures for improved cleavage fracture toughness. *Engineering Fracture Mechanics.* 2021, Vol. 253, p. 107878. https://doi.org/10.1016/j.engfracmech.2021.107878.

[8] Sun, G., et al. Effect of Rolling Temperature on Microstructural Characteristics and Deformation Mechanisms of a Metastable Austenitic Stainless Steel. *Steel Research International.* 2022, p. 2200096. https://doi.org/10.1002/srin.202200096.

[9] Jung, I., et al. Influence of the Cold Rolling and Annealing Sequence on the Ridging Behaviour of Ti-Stabilized 18% Cr Ferritic Stainless Steel. *Steel Research International.* 2010, Vol. 81, pp. 1089-1096. https://doi.org/10.1002/srin.201000125.

[10] Fuertes, N. and Pettersson, R. Effect of cold rolling on microstructure, corrosion and electrochemical response of the lean duplex stainless steel LDX 2101® by a correlative EBSD–SKPFM investigation. *Materials and Corrosion.* 2020, Vol. 71, pp. 1052–1065. https://doi.org/10.1002/maco.202011588.

[11] He, S. L., Liu, Y. and Jiang, D. M. Effect of martensite transformation on chemical composition, semiconductor property and corrosion resistance of passive film on SAE 304 stainless steel. *Materialwissenschaft und Werkstofftechnik.* 2018, Vol. 49, pp. 1455–1467. https://doi.org/10.1002/mawe.201800006.

[12] Maric, M., et al. The effect of cold-rolling on the microstructure and corrosion behavior of 316L alloy in FLiNaK molten salt. *Corrosion Science.* 2018, Vol. 142, pp. 133-144. https://doi.org/10.1016/j.corsci.2018.07.006.

[13] Nakhaie, D. and Moayed, M. H. Pitting corrosion of cold rolled solution treated 17-4 PH stainless steel. *Corrosion Science.* 2014, Vol. 80, pp. 290-298. https://doi.org/10.1016/j.corsci.2013.11.039.

[14] Salehi, M., et al. Comparison of the microstructure, corrosion resistance, and hardness of 321 and 310 s austenitic stainless steels after thermo-mechanical processing. *Materials Today Communications.* 2022, Vol. 31, p. 103638. https://doi.org/10.1016/j.mtcomm.2022.103638.

[15] Peguet, L., Malki, B. and Baroux, B. Influence of cold working on the pitting corrosion resistance of stainless steels. *Corrosion Science.* 2007, Vol. 49, pp. 1933-1948. https://doi.org/10.1016/j.corsci.2006.08.021.

[16] Parry, V., Col, A. and Pascal, C. Beneficial effect of cold-working on high temperature oxidation resistance of austenitic stainless steel. *Corrosion Science.* 2019, Vol. 160, p. 108149. https://doi.org/10.1016/j.corsci.2019.108149.

[17] Nezakat, M., et al. Effect of thermo-mechanical processing on oxidation of austenitic stainless steel 316L in supercritical water. *Corrosion Science.* 2015, Vol. 94, pp. 197-206. https://doi.org/10.1016/j.corsci.2015.02.008.

[18] Xin, S. S., et al. Effect of Temperature and Grain Size on the Corrosion Behavior of 316L Stainless Steel in Seawater. *Advanced Materials Research.* 2011, Vols. 299-300, pp. 175-178. https://doi.org/10.4028/www.scientific.net/AMR.299-300.175.

[19] Peguet, L., Malki, B. and Baroux, B. Effect of austenite stability on the pitting corrosion resistance of cold worked stainless steels. *Corrosion Science.* 2009, Vol. 51, pp. 493-498. https://doi.org/10.1016/j.corsci.2008.12.026.

[20] Pradhan, S.K., Bhuyan, P. and Mandal, S. Influence of the individual microstructural features on pitting corrosion in type 304 austenitic stainless steel. *Corrosion Science.* 2019, Vol. 158, p. 108091. https://doi.org/10.1016/j.corsci.2019.108091.

[21] Carvalho, R., et al. Effect of microstructure on the pitting susceptibility of a martensitic-ferritic stainless steel: A corrosion-metallurgical study. *Corrosion Science.* 2022, Vol. 202, p. 110277. https://doi.org/10.1016/j.corsci.2022.110277.

[22] ASTM A240-22. Standard Specification for Chromium and Chromium-Nickel Stainless Steel Plate, Sheet, and Strip for Pressure Vessels and for General Applications. *ASTM International.* 2022.

[23] Solomon, N. and Solomon, I. Effect of deformation-induced phase transformation on AISI 316 stainless steel corrosion resistance. *Engineering Failure Analysis.* 2017, Vol. 79, pp. 865-875. https://doi.org/10.1016/j.engfailanal.2017.05.031.

[24] Li, J., et al. Effect of microstructure on the corrosion resistance of 2205 duplex stainless steel. Part 1: Microstructure evolution during isothermal aging at 850ºC and evaluation of anticorrosion properties by methods of cyclic potentiodynamic polarization. *Construction and Building Materials.* 2018, Vol. 189, pp. 1286-1293. https://doi.org/10.1016/j.conbuildmat.2018.08.186.

[25] Chen, D., et al. Revealing the inner rules of PREN from electronic aspect by first-principles calculations. *Corrosion Science.* 2021, Vol. 189, p. 109561. https://doi.org/10.1016/j.corsci.2021.109561.

[26] Wang, D., et al. Comparison of 304 and 316 stainless steel microbiologically influenced corrosion by an anaerobic oilfield biofilm consortium. *Engineering Failure Analysis.* 2021, Vol. 122, p. 105275. https://doi.org/10.1016/j.engfailanal.2021.105275.

[27] De, A. K., et al. Quantitative measurement of deformation-induced martensite in 304 stainless steel by X-ray diffraction. *Scripta Materialia.* 2004, Vol. 50, pp. 1445-1449. https://doi.org/10.1016/j.scriptamat.2004.03.011.

[28] Xu, Y., et al. In situ X-ray diffraction study of martensitic transformation in austenitic stainless steel during cyclic tensile loading and unloading. *Scripta Materialia.* 2012, Vol. 67, pp. 771-774. https://doi.org/10.1016/j.scriptamat.2012.07.021.

[29] Raghavan, R., et al. Growth, structural, spectral, thermal, electrical and optical characterization of a novel optical material: Triethanolamine picrate single crystals for optical applications. *Chinese Journal of Physics.* 2020, Vol. 67, pp. 27-36. https://doi.org/10.1016/j.cjph.2019.11.017.

[30] ASTM G61-86. Standard Test Method for Conducting Cyclic Potentiodynamic Polarization Measurements for Localized Corrosion Susceptibility of Iron-, Nickel-, or Cobalt-Based Alloys. *ASTM International.* 2018.

[31] Yi, Y., et al. Potentiodynamic polarization behaviour of AISI type 316 stainless steel. *Corrosion Science.* 2013, Vol. 74, pp. 92-97. https://doi.org/10.1016/j.corsci.2013.04.028.

[32] Schvartzman, M. M. A. M., et al. Pitting Corrosion of Supermartensitic Stainless Steel in Chloride Solutions Containing Thiosulfate or H2S. *Journal of Materials Engineering and Performance.* 2018, Vol. 27, pp. 3723-3730. https://doi.org/10.1007/s11665-018-3403-x.

[33] Ha, H.-Y., et al. Enhancement of the resistance to localized corrosion of type 304 borated stainless steels through hot rolling. *Corrosion Science.* 2021, Vol. 192, p. 109798. https://doi.org/10.1016/j.corsci.2021.109798.

[34] Cruz, V., et al. Electrochemical studies on the effect of residual stress on the corrosion of 316L manufactured by selective laser melting. *Corrosion Science.* 2020, Vol. 164, p. 108314. https://doi.org/10.1016/j.corsci.2019.108314.

[35] ASTM G5-14. Standard Reference Test Method for Making Potentiodynamic Anodic Polarization Measurements. *ASTM International.* 2021.

[36] Ardila, M.A.N., et al. Influence of stainless steel specimen topography on micro-abrasion and micro-abrasion-corrosion. *Wear.* 2019, Vols. 426-427, pp. 1482-1495. https://doi.org/10.1016/j.wear.2019.01.011.

[37] Ma, G., et al. Effect of cold rolling on the corrosion behavior of Ta-4W alloy in sulphuric acid. *Corrosion Science.* 2020, Vol. 176, p. 108924. https://doi.org/10.1016/j.corsci.2020.108924.

[38] Sadeghi, F., et al. Role of the annealing twin boundary on the athermal α'-martensite formation in a 304 austenitic stainless steel. *Materialia.* 2021, Vol. 20, p. 101218. https://doi.org/10.1016/j.mtla.2021.101218.

[39] Lebedev, A.A. and Kosarchuk, V.V. Influence of phase transformations on the mechanical properties of austenitic stainless steels. *International Journal of Plasticity.* 2016, Vol. 16, pp. 749-767. https://doi.org/10.1016/S0749-6419(99)00085-6.

[40] Li, J., et al. Study of Cold Rolling on the Transformation Mechanism Microstructure, and Properties of 304 Austenitic Stainless Steel. *Steel Research International.* 2022, Vol. 93, p. 2100341. https://doi.org/10.1002/srin.202100341.

[41] Corrêa, E. C. S., Aguilar, M. T. P. and Cetlin, P. R. The influence of cyclic straining on the work hardening behavior of AISI 304 stainless steel bars in multiple-pass drawing. *Materials Chemistry and Physics.* 2007, Vol. 106, pp. 95-101. https://doi.org/10.1016/j.matchemphys.2007.05.025.

[42] Liu, H., et al. XRD and EBSD studies of severe shot peening induced martensite transformation and grain refinements in austenitic stainless steel. *Materials Characterization.* 2020, Vol. 168, p. 110574. https://doi.org/10.1016/j.matchar.2020.110574.

[43] Mohammadi, F. and Luo, J. Effect of cold work on erosion–corrosion of 304 stainless steel. *Corrosion Science.* 2011, Vol. 53, pp. 549-556. https://doi.org/10.1016/j.corsci.2010.09.059.

[44] Guan, L., et al. Effects of cyclic stress on the metastable pitting characteristic for 304 stainless steel under potentiostatic polarization. *Corrosion Science.* 2015, Vol. 93, pp. 80-89. https://doi.org/10.1016/j.corsci.2015.01.009.

[45] Vasudevan, S. Studies Relating To Cathodic Reactions In Neutral Chloride Solutions Used In Chlorate Processes. *Industrial & Engineering Chemistry Research.* 2008, Vol. 47, pp. 5742-5745. https://doi.org/10.1021/ie800038f.

[46] Barbucci, A., Cerisola, G. and Cabot, P. L. Effect of cold working in the passive behavior of 304 stainless steel in sulfate media. *Journal of Electrochemical Society.* 2002, Vol. 149, pp. 534-542. https://doi.org/10.1149/1.1516774.

[47] Izquierdo, J., et al. Scanning microelectrochemical characterization of the effect of polarization on the localized corrosion of 304 stainless steel in chloride solution. *Journal of Electroanalytical Chemistry.* 2014, Vol. 728, pp. 148-157. http://dx.doi.org/10.1016/j.jelechem.2014.06.009.

[48] Li, J., et al. Study on pitting corrosion behavior and semi in-situ pitting corrosion growth model of 304 L SS with elastic stress in NaCl corrosion environment. *Corrosion Science.* 2023, Vol. 211, p. 110862. https://doi.org/10.1016/j.corsci.2022.110862.

[49] Phadnis, S. V., et al. Comparison of rolled and heat treated SS304 in chloride solution using electrochemical and XPS techniques. *Corrosion Science.* 2003, Vol. 45, pp. 2467-2483. https://doi.org/10.1016/S0010-938X(03)00099-4.

[50] Kashani, F. R. and Rezaei, M. Electrochemical studies and molecular simulations on the use of molybdic acid for stabilization of AISI 304 stainless steel passive film in sulfuric acid medium. *Journal of Molecular Liquids.* 2021, Vol. 344, p. 117733. https://doi.org/10.1016/j.molliq.2021.117733.

[51] Lodhi, M. J. K. , et al. Microstructural features contributing to macroscopic corrosion: The role of oxide inclusions on the corrosion properties of additively manufactured 316L stainless steel. *Corrosion Science.* 2022, Vol. 203, p. 110354. https://doi.org/10.1016/j.corsci.2022.110354.

[52] Chang, L., et al. The effect of martensite on stress corrosion crack initiation of austenitic stainless steels in high-temperature hydrogenated water. *Corrosion Science.* 2021, Vol. 189, p. 109600. https://doi.org/10.1016/j.corsci.2021.109600.

[53] Tsay, L. W., Lin, Y. J. and Chen, C. The effects of rolling temperature and sensitization treatment on the sulfide stress corrosion cracking of 304L stainless steel. *Corrosion Science.* 2012, Vol. 63, pp. 267-274. https://doi.org/10.1016/j.corsci.2012.06.008.

[54] Wang, C., et al. Microstructure evolution and corrosion behavior of dissimilar 304/430 stainless steel welded joints. *Journal of Manufacturing Processes.* 2020, Vol. 50, pp. 183-191. https://doi.org/10.1016/j.jmapro.2019.12.015.

[55]   Li, W., et al. Promotion of pitting corrosion at hydrogen-enriched α/γ phase boundaries in austenitic stainless steel weld joints. *Acta Materialia.* 2022, Vol. 277, p. 117728. https://doi.org/10.1016/j.actamat.2022.117728.

[56]   Houmard, M., et al. Surface physico-chemistry study of an austenitic stainless steel: Effect of simple cold rolling treatment on surface contamination. *Corrosion Science.* 2007, Vol. 49, pp. 2602-2611. https://doi.org/10.1016/j.corsci.2006.12.016.